Review Article

Blind spots in brain imaging: a pictorial essay

Mengwen Liu[1#], Xin Wen[1#], Meng Li[1], Qiang Huang[2], Chengyi Jiang[1], Jiuming Jiang[1], Li Zhang[1*], Hongmei Zhang[1*]

[1]Department of Diagnostic Radiology, National Cancer Center/National Clinical Research Center for Cancer/Cancer Hospital, Chinese Academy of Medical Sciences and Peking Union Medical College, Beijing, China; [2]Department of Radiology, the First Affiliated Hospital, Zhejiang University School of Medicine, Hangzhou, China

Contributions: (I) Conception and design: L Zhang, H Zhang; (II) Administrative support: L Zhang, H Zhang; (III) Provision of study materials or patients: M Liu, X Wen, M Li; (IV) Collection and assembly of data: M Li, C Jiang, J Jiang; (V) Data analysis and interpretation: M Liu, X Wen; (VI) Manuscript writing: All authors; (VII) Final approval of manuscript: All authors.

[#]These authors contributed equally to this work as co-first authors.

*These authors contributed equally to this work.

Correspondence to: Li Zhang, MD; Hongmei Zhang, MD. Department of Diagnostic Radiology, National Cancer Center/National Clinical Research Center for Cancer/Cancer Hospital, Chinese Academy of Medical Sciences and Peking Union Medical College, No. 17 Panjiayuannanli, Chaoyang District, Beijing 100021, China. Email: zhangli_cicams@163.com; 13581968865@163.com.

Abstract: Currently, radiologists must interpret large quantities of images and identify diseases on a daily basis. The minimization of errors is crucial for high-quality diagnostic imaging and optimal patient care. Brain imaging is frequently used in clinical practice; however, radiologists are prone to overlook some regions in brain imaging and make perceptual errors, thus leading to missed diagnoses. These regions, also known as "blind spots", comprise a number of intricate areas, including the posterior fossa, cerebral sulci and pia mater, cranial nerves (CNs), intracranial arteries, dural sinuses, sella and parasellar region, Meckel's cave, skull base, scalp, orbit, and pterygopalatine fossa (PPF). Therefore, the knowledge of normal computed tomography (CT) and magnetic resonance imaging (MRI) manifestations and common lesions in these blind spots is imperative to avoid false-negative results. This article graphically discusses and analyzes these common blind spots of brain imaging using real representative cases. It also provides comprehensive strategies to address missed diagnostic errors in radiology, including enhancing the selection of imaging protocols, implementing a multi-reviewer reporting system, adopting structured reporting templates, employing error measurement or detection strategies, and promoting the use, development, and refinement of artificial intelligence (AI) to improve diagnostic accuracy and efficiency. This article may also increase junior doctors' awareness of these blind spots and assist them in their daily work, and thus has continuing education implications.

Keywords: Brain imaging; blind spots; missed diagnosis

Submitted Jun 24, 2024. Accepted for publication Nov 14, 2024. Published online Dec 30, 2024.
doi: 10.21037/qims-24-1270
View this article at: https://dx.doi.org/10.21037/qims-24-1270

Introduction

Medical imaging plays a critical role in medical diagnosis and treatment, including screening, disease diagnosis, and efficacy evaluation. However, diagnostic imaging errors and biases are common in the radiology department, and negatively affect patient care. Errors by radiologists in image interpretation are frequently classified as either perceptual or cognitive. The term "miss" refers to a failure to notice a significant finding, which is how perceptual errors are typically described. Conversely, cognitive errors can be viewed as misunderstandings, where an imaging abnormality is found, but an incorrect disease diagnosis is made (1). Therefore, radiologists must strive to minimize perceptual and cognitive mistakes to ensure accurate diagnosis and improve patient care.

Perceptual errors happen with greater frequency than cognitive errors in daily practice (70% *vs.* 30%) (2,3). Consequently, preventing missed diagnoses is imperative for patient care, particularly given the significant increase in the overall volume of image readings. Fatigue and insufficient time to read images can both lead to perceptual errors. Additionally, specific anatomical areas are often overlooked during image review, leading to a higher likelihood of missed diagnoses. These overlooked regions are commonly referred to as "blind spots". Understanding and paying attention to imaging anatomy and common lesions in these "blind spots" could help to reduce the missed diagnosis rate.

Brain imaging is regularly used to perform clinical examinations of patients with neurological symptoms and to stage patients with malignant tumors. Computed tomography (CT) and magnetic resonance imaging (MRI) are the primary imaging methods for the head. However, there are blind spots in the head that can be easily missed, such as the posterior fossa, pia mater, dural sinuses, cavernous sinuses, clivus, Meckel's cave, skull base, orbit, and cervicofacial structure [e.g., pterygopalatine fossa (PPF)]. To avoid false-negative results, these blind spots must be carefully evaluated in each brain imaging test. Knowledge of typical CT and MRI presentations, and the anatomical characteristics of these blind areas is also of vital significance, and care should be taken to avoid false-positive results.

In this article, we discuss and illustrate blind spots in brain imaging in the normal anatomy, potential interpretive flaws, and differential diagnosis with the aim of reducing the likelihood of missed diagnoses in routine brain imaging in clinical work.

Common blind spots in brain imaging

Posterior fossa

The posterior fossa is an especially important space in the cranial cavity. It is mainly separated from other structures by the anatomical structures of the skull. The occipital bones, the petrous portion of the temporal bone, and other bones make up the fossa base. It communicates downward with the vertebral canal through the foramen magnum of the occipital bone, and the fossa roof is the tentorium cerebelli, which communicates upward with the other portions of the cranial cavity through the hiatus of the tentorium cerebelli. The posterior cranial recess mainly contains important structures, such as the cerebellum, the brainstem, the fourth ventricle, the cerebellopontine angle (CPA) cistern, the midbrain pool (including the interpeduncular fossa and the ambient cisterns), and the pontine cistern (which contains the basilar artery). The brainstem includes the midbrain, pons, and medulla oblongata. The posterior fossa is surrounded by bone, and sclerotic artifacts of bone density on CT tend to obscure some of the anatomical details of the posterior fossa. Additionally, a portion of the posterior fossa may be observed in neck CT, and certain posterior fossa lesions can incidentally be observed in neck CT, which is a blind spot and an easily missed area (*Figure 1*). The structures in the posterior fossa can be observed clearly on axial and sagittal MRI images.

Congenital abnormalities, neoplastic lesions, inflammatory demyelinating diseases, and infectious and vascular diseases comprise the majority of posterior fossa diseases. Among different types of congenital malformations, Arnold-Chiari malformation, and Dandy-Walker syndrome are commonly detected in the examination of the cerebellum and the fourth ventricle. Extra-axial CPA lesions arising from the CPA and its contents mainly include vestibular and non-vestibular schwannomas, meningiomas, metastases, aneurysms, tuberculosis, and various other meningeal lesions (4), while intra-axial lesions mainly include lymphomas, gliomas, and metastatic tumors (5). Conversely, in the cerebellum and fourth ventricle region, tumors in or around the brain and ventricles are predominant, such as astrocytomas, medulloblastomas, ventricular meningiomas, hemangioblastomas, ependymomas, metastatic tumors, and lymphomas. Brainstem tumors, the most common type of which is glioma, are less frequent.

Inflammatory demyelinating diseases mainly include multiple sclerosis (MS) and acute disseminated encephalomyelitis (ADEM), both of which can appear anywhere in the central nervous system (CNS) (6), and first-onset MS and ADEM need to be distinguished from each other. One crucial distinguishing factor is that the MRI features of ADEM typically include widespread, bilateral, and asymmetric involvement of supratentorial and

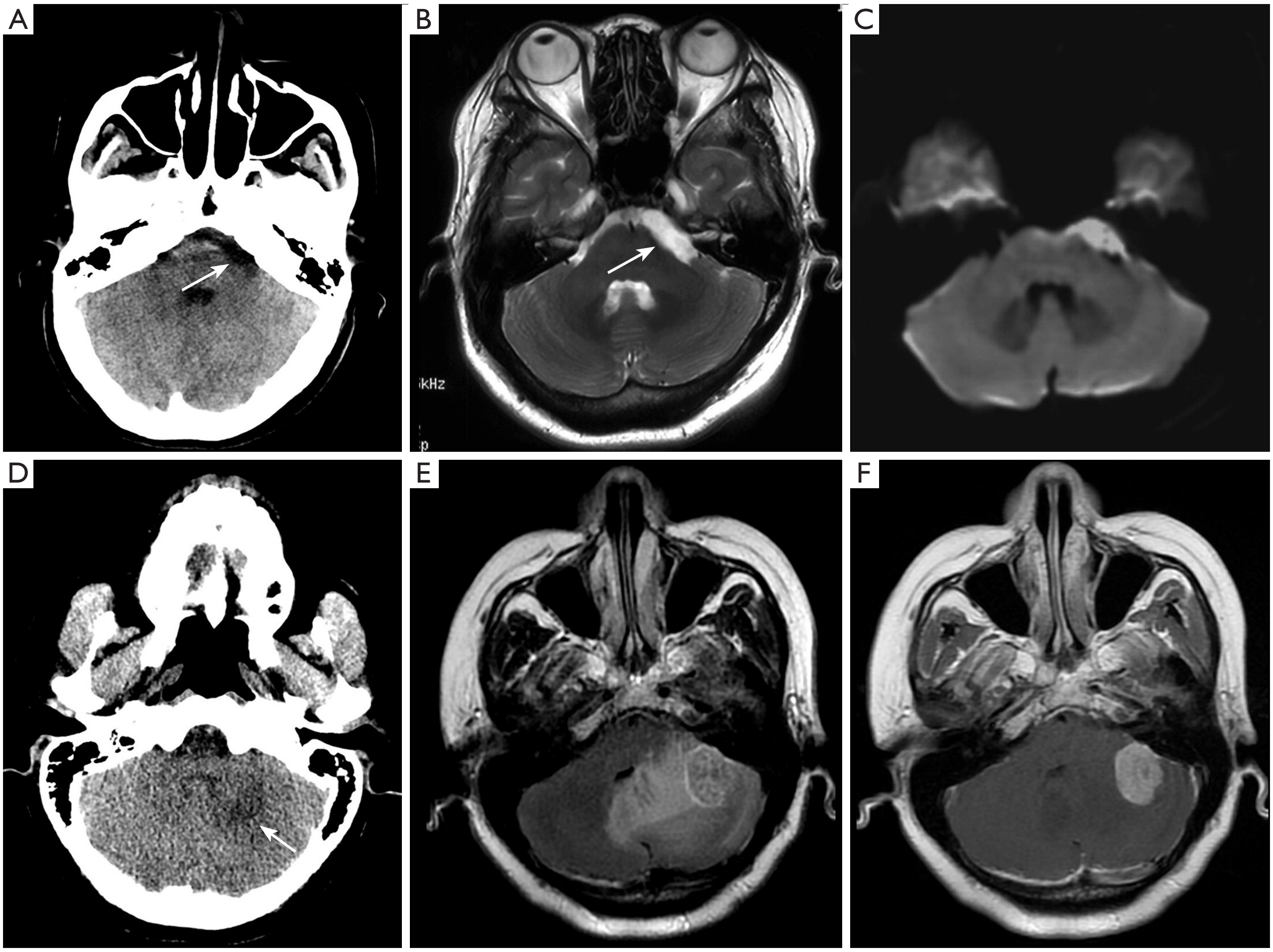

Figure 1 Blind spot in brain imaging: posterior fossa. (A-C) Scans of a 34-year-old female who had experienced left facial pain for one year. (A) CT images revealed a low-density lesion (arrow) in the anterior aspect of the brainstem, extending into the left pontocerebellar angle region. (B,C) In the brain MRI examination, the lesion displayed high signal intensity on T_2WI/FLAIR (arrow) (B) with restricted diffusion on DWI (C). Finally, postoperative pathology confirmed the diagnosis of an epidermoid cyst. (D-F) Scans of a 53-year-old female with lymph node metastasis who had undergone surgery for right breast cancer, and 2 months of postoperative chemotherapy. (D) Radiologists overlooked a low-density lesion in the left cerebellum (arrow) in the neck and chest CT scan, (E,F) which was later shown to be a metastatic tumor by MRI. Neck CT scans can include the posterior fossa; however, this crucial region tends to be disregarded by radiologists. Therefore, importance should be attached to this area in image interpretation. CT, computed tomography; MRI, magnetic resonance imaging; T_2WI/FLAIR, T2-weighted image/fluid-attenuated inversion recovery; DWI, diffusion-weighted imaging.

infratentorial white matter, deep gray nuclei, and the spinal cord (7). The posterior fossa can also be affected by vascular disorders (e.g., an infarction or hemorrhage) and infectious disorders (e.g., encephalitis, brain abscesses, and cysticercosis), which eventually induce neoplastic space-occupying lesions. The specific diagnosis of lesions relies heavily on corresponding clinical symptoms and imaging characteristics. Asymmetric narrowing and the absence of the cisterns are two indirect space-occupying signals that are frequently used in CT to indicate a lesion. Further, if a mass lesion is suspected on CT, contrast-enhanced MRI with specific protocols needs to be implemented for further evaluation (8).

Cerebral sulci and pia mater

The cerebral sulci, as opposed to the gyri, are slit-like parts of the pallium. The pia mater is the cerebral tegument's innermost layer, which adheres to the brain's surface and

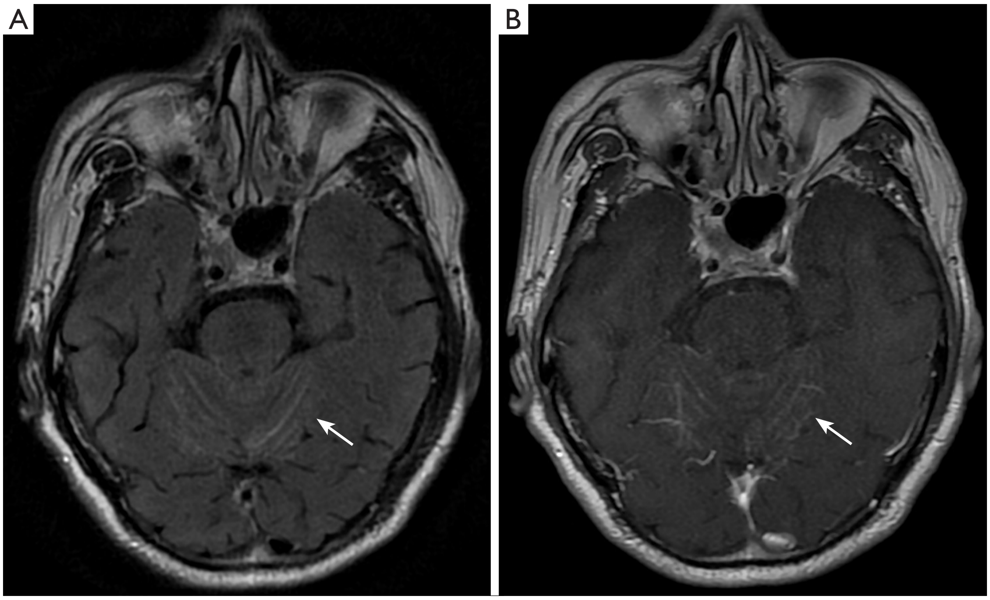

Figure 2 Blind spot in brain imaging: cerebral sulci and pia mater. Scans of a 62-year-old male who had experienced head distending pain for 2 months after chemotherapy for right lower lobe adenocarcinoma. Brain MRI showed multiple linear abnormal signals in the bilateral cerebellar vermis (arrows). These lesions were hyperintense on T_2WI/FLAIR (A) and markedly enhanced on the enhanced scan (B), demonstrating the leptomeningeal metastasis. Compared to parenchymal metastasis, metastasis involving the leptomeninge is highly likely to be overlooked. MRI, magnetic resonance imaging; T_2WI/FLAIR, T2-weighted image/fluid-attenuated inversion recovery.

follows the gyri into the sulci (9). The subarachnoid space, which contains cerebrospinal fluid (CSF), separates the pia mater from the overlying arachnoid mater. However, the pia mater, subarachnoid space, and arachnoid mater are indistinguishable on imaging. It is strongly recommended that MRI be used to assess the sulci and the pia mater. Notably, fluid-attenuated inversion recovery (FLAIR) images of T_2-weighted images (T_2WI), pre and post contrast, are of particular value in the diagnosis of the sulci and the pia mater (10). Among the sequences, contrast-enhanced FLAIR is the most sensitive sequence for diagnosing meningitis (11).

On MRI T_2WI/FLAIR, hyperintensity of the cerebral sulcus is a typical sign of many neurological disorders, such as subarachnoid hemorrhage (SAH) (12). When T_2WI/FLAIR imaging displays abnormal hyperintensity in the cerebral sulci, further contrast enhancement is required to confirm the disease involving the pia mater (13). Pia mater lesions mainly include diseases such as meningitis and meningeal metastases. Meningeal metastases, also known as carcinomatous meningitis, are the most common form of meningeal cancer involvement. Enhanced MRI images can show nodular, curved linear enhancement of the invaded meninges, which may extend into the sulci and cisterns (*Figure 2*) (13). On plain CT, the sulci appear as water-like with low density. If the sulci are hyperdense, it may indicate adjacent SAH or meningeal diseases. Compared with the parenchyma, sulci and pia mater abnormalities are easy to miss. Therefore, radiologists should pay special attention to these manifestations.

Cranial nerves (CNs)

There are 12 pairs of CNs: olfactory (CN I), optic (CN II), oculomotor (CN III), trochlear (CN IV), trigeminal (CN V) and its three main branches [ophthalmic (CN V_1), maxillary (CN V_2) and mandibular (CN V_3)], abducens (CN VI), facial (CN VII), auditory (CN VIII), glossopharyngeal (CN IX), vagus (CN X), accessory (CN XI), and hypoglossal (CN XII) (14). CN I is connected to the telencephalon; CN II terminates at the intracranial optic chiasm; CN III and CN IV originate in the midbrain; CN V–VIII originate in the pons; CN IX–XII originate in the medulla oblongata. The apertures through which the CNs exit the skull are shown in the section *Skull base* (*Table 1*).

In imaging, MRI is considered the gold standard in the study of CNs. CNs have distinct features on MRI sequence imaging. T1-weighted image (T_1WI) can be used to provide anatomical definition, assess surrounding fat invasion, and

Table 1 Skull base foramina, transmitted contents, and connections

Aperture	Contents	Connections
Olfactory foramina	CN I	Anterior fossa-superior nasal cavity
Optic canal	CN II	Orbital apex-middle fossa
Superior orbital fissure	CN III, IV, V1, VI; superior ophthalmic vein	Orbit-middle fossa
Foramen rotundum	CN V_2	Meckel's cave-pterygopalatine fossa
Foramen ovale	CN V_3	Meckel's cave-infratemporal fossa
Foramen spinosum	Middle meningeal artery	Middle fossa-infratemporal fossa
Foramen lacerum/carotid canal	Meningeal branches of the ascending pharyngeal artery, ICA	Internal carotid interval-cavernous sinus
Vidian canal	Vidian artery and nerve	Foramen lacerum-pterygopalatine fossa
Jugular foramen	CN IX, X, XI, internal jugular vein	Posterior fossa-nasopharyngocarotid space
Stylomastoid foramen	CN VII	Parapauricular space-middle ear
Hypoglossal canal	CN XII	Foramen magnum-nasopharyngocarotid space
Foramen magnum	Medulla	Posterior fossa-neck canal

CN, cranial nerve; ICA, internal carotid artery.

identify denervation changes. Conversely, T_2WI can be used to characterize lesions, evaluate CSF space patency, and detect denervation changes. Moreover, fast-spin echo and steady-state free procession sequences are effective at visualizing the cisternal course of nerves and identifying neurovascular conflicts. In addition, DWI and FLAIR sequences can be used to detect ischemic lesions, while a post-gadolinium T_1WI with fat-suppression technique is essential for detecting nerve enhancement, perineural spread (PNS), and meningeal infiltration (15).

Frequently observed lesions affecting CNs include traumatic, vascular, inflammatory (both infectious and non-infectious), and neoplastic lesions (16). In imaging examinations, lesions triggered by traumatic, vascular, and inflammatory diseases often show non-specific swelling and enhancement of the affected nerve. Neoplastic lesions include olfactory neuroblastoma in the olfactory nerve, glioma, and meningioma in the optic nerve, as well as schwannomas, which are commonly found in the auditory and trigeminal nerves, and PNS, which is usually observed in the second and third branches of the trigeminal nerve, and lymphomas (*Figure 3*) (17,18). MRI, particularly enhanced MRI, is primarily employed for the localization and diagnosis of CN abnormalities, while CT is used for the evaluation of nearby bones. Due to the intricacy of cerebral neuroanatomy, radiologists should assess CNs and the adjacent structures when rarely seen CN relevant signs are observed (16,18,19).

Intracranial arteries

The intracranial arteries are critical components of the cerebral vascular system, supplying oxygenated blood to the brain. These arteries include the internal carotid arteries (ICAs) and the vertebral arteries. ICAs are anatomically divided into seven segments and bifurcate into the anterior and middle cerebral arteries (MCAs). The bilateral vertebral arteries converge to form the basilar artery. The anterior cerebral artery primarily supplies the medial aspects of the frontal lobes and the superior medial parietal lobes, while the MCA provides blood to the lateral surfaces of the frontal, temporal, and parietal lobes. The basilar artery supplies the brainstem, cerebellum, and posterior part of the cerebral hemisphere.

Intracranial arteries are susceptible to a range of pathological conditions that can have significant clinical implications, such as stenosis, atherosclerosis (20), aneurysms (21), and vasculitis (22) (*Figure 4*). For patients with cerebral infarction, it is important to pay close attention to the stenosis of the responsible artery (*Figure 4*). The MCA sign refers to the abnormal hyperdense appearance of the MCA on non-contrast CT in patients with acute cerebral infarction. This sign is indicative of thrombus or occlusion in the MCA trunk, and is an early imaging marker of acute ischemic stroke. Basilar artery thrombosis is a potentially catastrophic condition that is frequently overlooked in both clinical and radiologic evaluations, as it runs along the ventral surface of the pons, which is itself a common

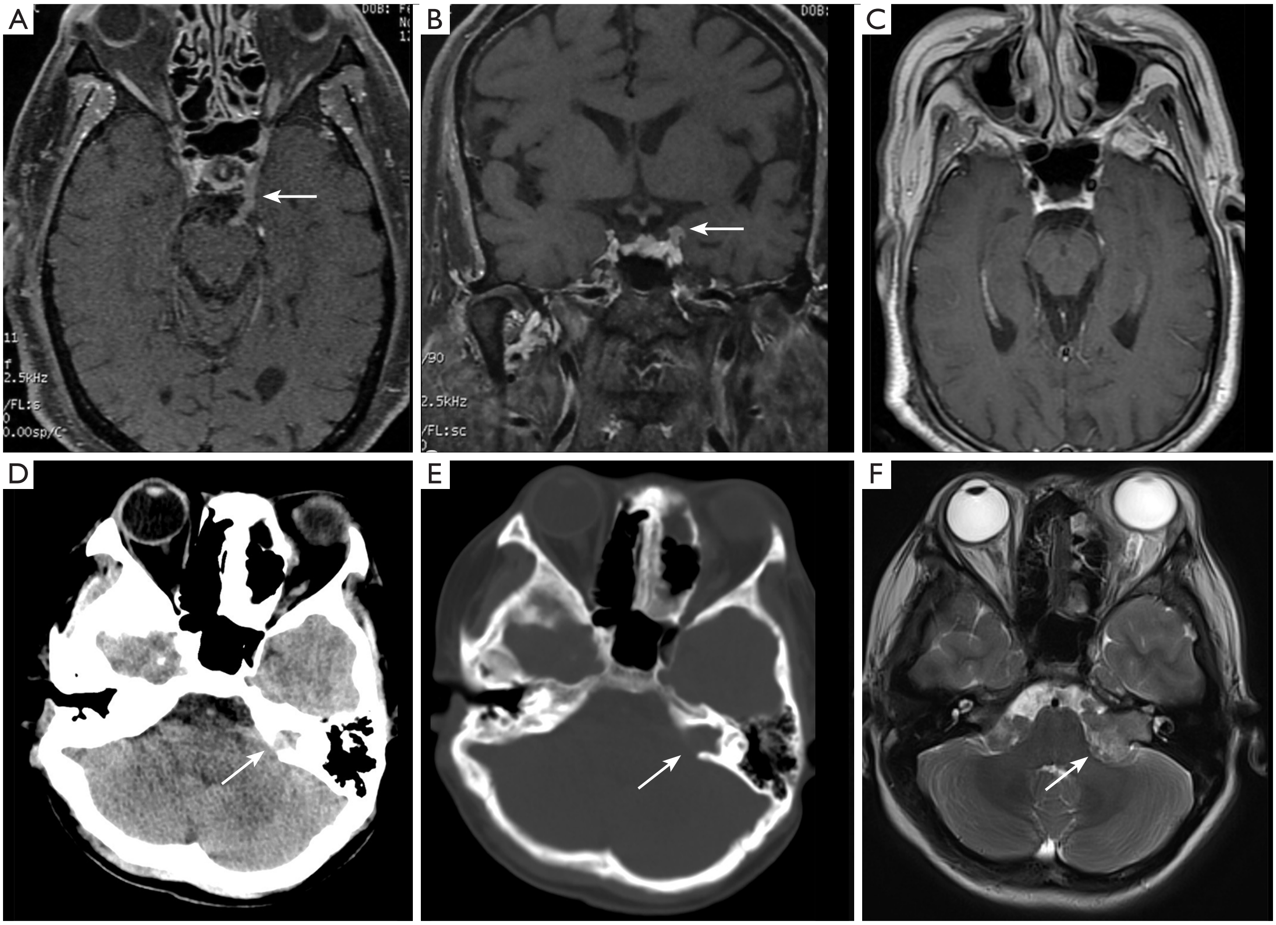

Figure 3 Blind spot in brain imaging: cranial nerves. (A-C) Scans of a 65-year-old male with lymphoma and ptosis of the left eye. (A,B) Axial and coronal enhanced MRI showed thickening and enhancement of the left oculomotor nerve (arrows). Taking into account the specific clinical presentations of this patient, a diagnosis of lymphoma affecting the oculomotor nerve was considered. (C) After chemotherapy, the previously thickened oculomotor nerve returned to normal. (D-F) Scans of a 20-year-old female after surgery for neurofibromatosis. (D,E) CT scan showed an enlargement of the left internal auditory canal (arrows), suggesting a pathological condition in the left internal auditory canal region. (F) MRI revealed multiple abnormal signal masses and nodules in the bilateral cerebellopontine angles, pons, and medulla oblongata. Among them, the largest lesion was located in the left cerebellopontine angle (arrow), extending along the facial nerve to the internal auditory canal, with localized canal enlargement. Ultimately, a diagnosis of multiple neurofibromas was made. MRI, magnetic resonance imaging; CT, computed tomography.

anatomical blind spot in brain imaging (21). The window of opportunity for intervention in cases of basilar artery thrombosis is extremely narrow; thus, every radiologist who interprets CT examinations of the brain should include the basilar artery on the checklist of anatomical areas to review.

Dural sinuses

Dural sinuses are blood-containing spaces generated by the separation of the inner and outer layers of the dura mater, which receive blood from the brain's superficial and deep venous systems (23), ultimately infusing into the internal jugular vein. The major dural sinuses include the superior sagittal sinus, inferior sagittal sinus, inferior petrosal sinus, sinus confluence, transverse sinus, and sigmoid sinus. The superior sagittal sinus is located at the superior edge of the falx cerebri, and converges posteriorly into the sinus confluence. At the lower margin of the falx cerebri, the inferior sagittal sinus converges backward into the straight sinus in the same way as the superior sagittal sinus. The

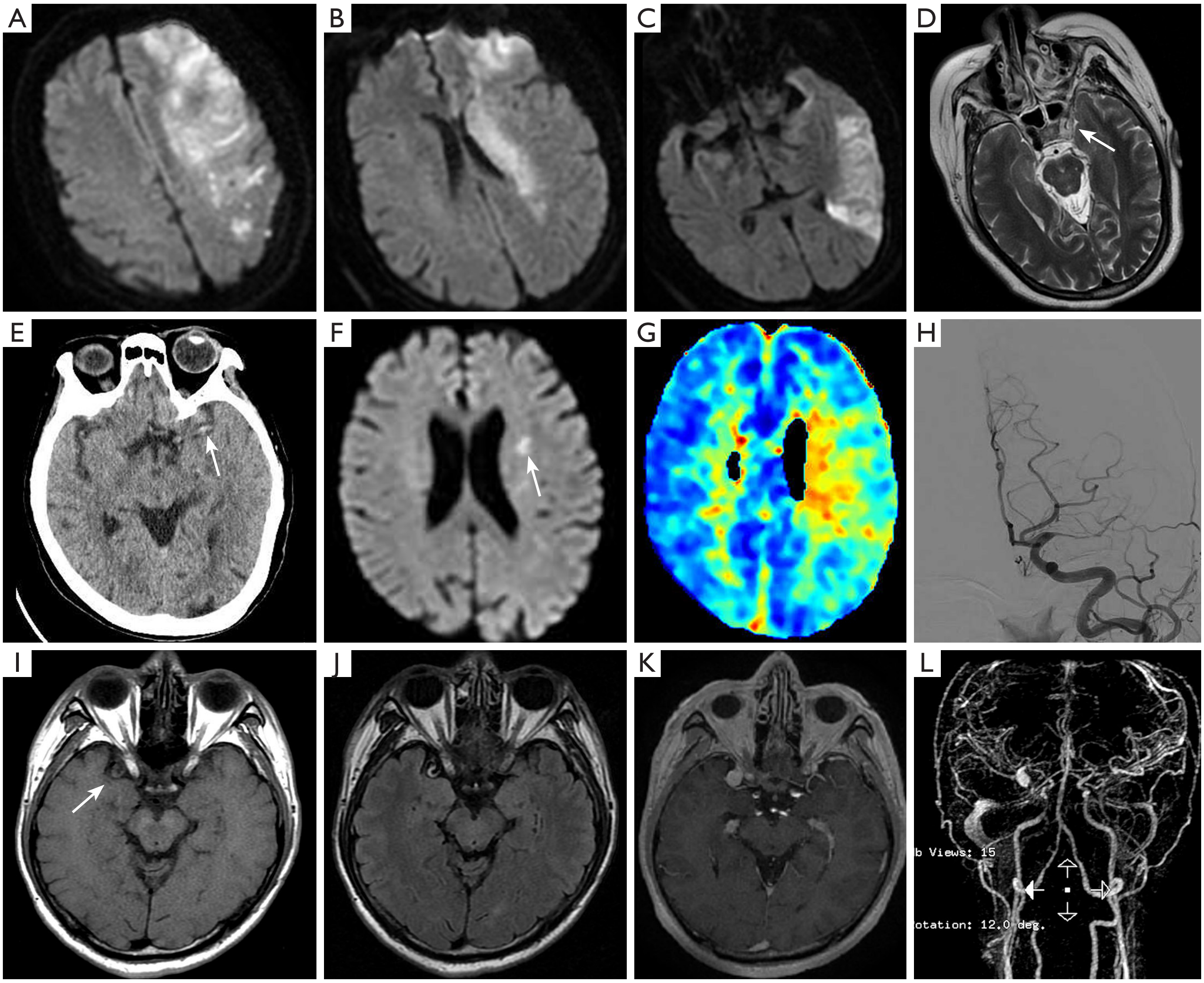

Figure 4 Blind spot in brain imaging: intracranial arteries. (A-D) Scans of a 49-year-old female after endometrial cancer surgery. During the follow-up period, the patient developed neurological symptoms such as excessive sleepiness, muscle weakness, sensory loss, an inability to frown and protrude the tongue, and the disappearance of the nasolabial fold, which highly indicated an intracranial lesion. (A-C) MRI showed multiple wedge-shaped and patchy abnormal signal lesions in the blood-supply area of the left anterior and MCAs. The lesions were hyperintense in T_2WI/FLAIR and DWI, suggesting a diagnosis of cerebral infarction. (D) Additionally, abnormal signals in the internal carotid artery were observed in the region of the cavernous sinus (arrow), suggesting thrombus formation. (E-H) Scans of a 73-year-old female with left-sided cerebral infarction. (E) CT showed the hyperdense sign in the middle cerebral artery (arrow). (F) DWI showed high signal lesions on the left side (arrow), (G) PWI showed prolonged MTT in the left cerebral hemisphere, and (H) DSA showed middle cerebral artery stenosis. (I-L) Scans of a 63-year-old male with eminence of the left face accompanied by reduced facial sensation after radiotherapy for right maxillary sinus cancer. (I-K) The aneurysmal dilation near the orbital apex adjacent to the right cavernous sinus was shown by MRI (arrow). (L) Ultimately, brain MRA showed an aneurysm in the M1 segment of the middle cerebral artery. MRI, magnetic resonance imaging; MCA, middle cerebral artery; T_2WI/FLAIR, T2-weighted image/fluid-attenuated inversion recovery; DWI, diffusion-weighted imaging; CT, computed tomography; PWI, perfusion weighted imaging; MTT, mean transit time; DSA, digital subtraction angiography; MRA, magnetic resonance angiography.

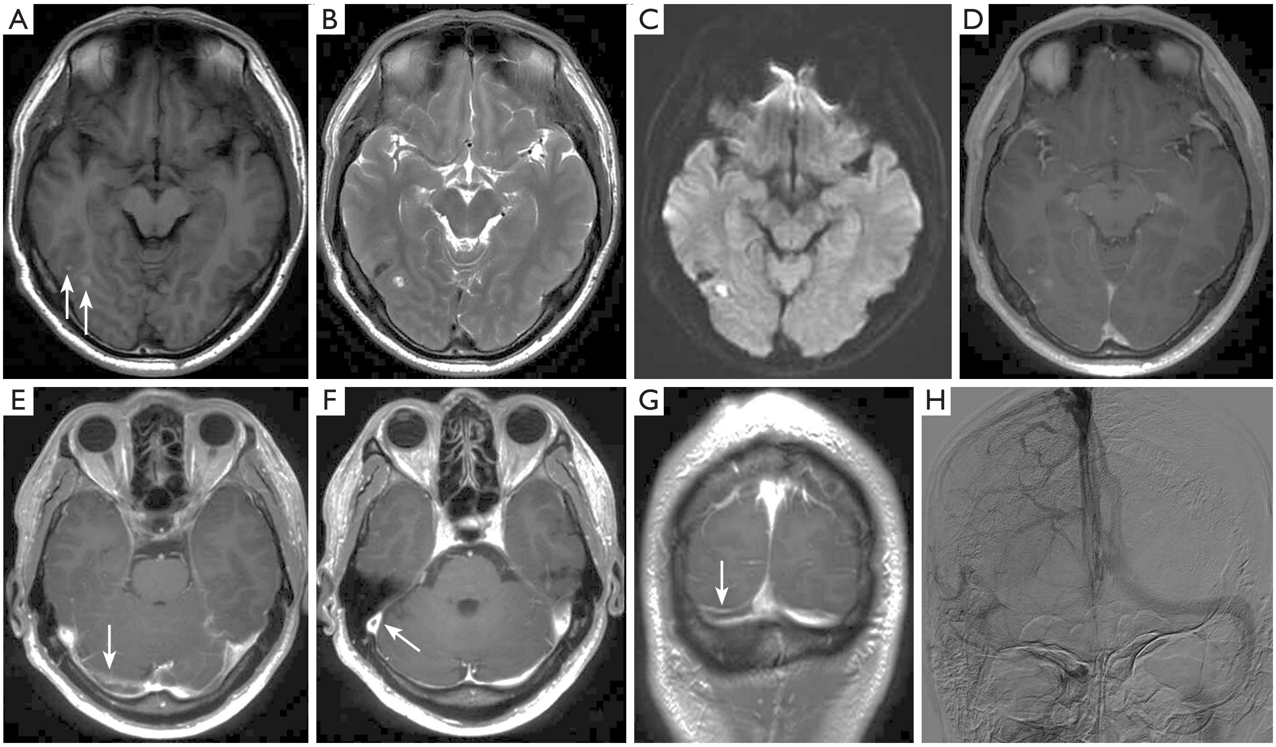

Figure 5 Blind spot in brain imaging: dural sinuses. Scans of a 42-year-old male with a 2-week headache and dizziness. (A-D) MRI showed two nodular abnormal signals in the right temporo-occipital lobe (arrows). Given the signal characteristics, radiologists diagnosed them as hemorrhagic foci. (E-G) MRI T_2WI/FLAIR showed hypointense lesions within the right transverse sinus and straight sinus (arrows). (H) DSA confirmed the presence of a venous sinus thrombosis. The final diagnosis was secondary intracranial hemorrhage following CVST. MRI, magnetic resonance imaging; T_2WI/FLAIR, T2-weighted image/fluid-attenuated inversion recovery; DSA, digital subtraction angiography; CVST, cerebral venous sinus thrombosis.

straight sinus is located at the junction of the falx cerebri and the tentorium cerebelli, and drains the inferior sagittal sinus and the deep venous system to the sinus confluence. The sinus confluence converges with the superior sagittal sinus and the straight sinus, and moves laterally to the transverse sinus. The sigmoid sinus is a continuation of the transverse sinus and joins the internal jugular vein at the jugular foramen. Notably, the cavernous sinus comprises a pair of specialized dural sinuses located on either side of the sella turcica at the base of the skull. It also belongs to the parasellar region, and relevant details can be found in the *Sella and parasellar region* section of this article.

The most common abnormality involving the dural sinuses is cerebral venous sinus thrombosis (CVST) (23). The etiology of CVST is complicated; risk factors range from thrombosis-prone conditions related to pregnancy and taking oral contraceptives to infections, trauma, and tumor compression. The current gold standard for depicting CSVT combines conventional MRI with magnetic resonance venography (MRV), and uses dynamic time-resolved angiographic techniques, such as time-resolved imaging of contrast kinetics (TRICKS) and time-resolved imaging with stochastic trajectories. TRICKS employs rapid acquisitions to deliver dynamic images of intravascular contrast flow. This technique offers excellent spatial resolution and dynamic flow information that previously required more invasive procedures, such as interventional angiography (24).

Currently, in clinical work, the diagnosis of CVST is mainly based on CT and computed tomography venography (CTV), MRI, and MRV. On CT plain scan, CVST may manifest as localized hyperdensity of the dural venous sinus, the triangular sign, the striated sign, etc. MRI signals change depending on when the thrombosis occurs. CTV or MRV show filling defects (*Figure 5*). Indirect imaging signs of CVST that are relied on to provide diagnoses include cerebral edema, venous infarction, and hemorrhage. Differential diagnoses include venous sinus hypoplasia, and arachnoid granulations. CVST is a rare cerebrovascular disease with a non-specific clinical syndrome, and is thus easily missed in diagnosis. Dural sinuses are also exceedingly difficult to assess on imaging, particularly on non-enhanced brain CT (25). Therefore, when analyzing images, radiologists should focus on the lesions in this area (23).

Sella and parasellar region

The sella turcica, a concave depression in the basisphenoid bone that houses the pituitary gland, is bordered anteriorly by the tuberculum sellae and the anterior clinoid processes, and posteriorly by the dorsum sellae and the posterior clinoid processes. The pituitary gland itself is composed of the adenohypophysis, which represents the larger anterior portion (70–80%), and the neurohypophysis, which is located posteriorly. On T_1WI and T_2WI, the adenohypophysis appears isointense to gray matter. However, the neurohypophysis exhibits high signal intensity on T_1WI, which is associated with the storage of antidiuretic hormone within it.

Pituitary adenomas are the most common sellar region tumors, accounting for about 80% of sellar tumors and 10–15% of intracranial tumors (26). Tumors 10 mm or larger in size are macroadenomas, while smaller tumors are microadenomas. Clinically, adenomas are classified as either functional or nonfunctional. Functional adenomas are rarely missed, but nonfunctional adenomas, especially microadenomas, are often missed on CT scans. Other conditions like pituitary apoplexy, hyperplasia, hypophysitis, sarcoidosis, histiocytosis, and pituitary carcinoma are less common; thus, it is essential to focus on this region during imaging (26). Pituitary metastases comprise 1.0–3.6% of all surgically treated pituitary lesions. Consequently, in patients with a history of malignancy, heightened awareness for potential metastases to the pituitary gland and stalk is essential (27) (*Figure 6*).

The parasellar region is a general term referring to the surrounding structures, such as the cavernous sinuses laterally and the suprasellar cistern structures above the pituitary gland. The cavernous sinus, a pair of significant dural sinuses located on two sides of the sphenoid sinus and pituitary gland, is also a common anatomical blind spot in image diagnosis. Coronal high-resolution MRI show the nerves that run along the lateral wall as medium signals, among which, the oculomotor nerve is displayed the best. MRI with and without contrast is the preferred imaging modality for suspected sellar or parasellar pathologies.

Lesions in the parasellar region can originate from various structures, including those in the cavernous sinus and other areas. Lesions that frequently originate from the cavernous sinus include meningiomas and schwannomas. Vascular lesions are also common in this area, and include ICA-cavernous sinus fistulae, arterial stenosis, aneurysms, and hemangiomas (28,29). Aneurysms in the cavernous sinus account for 2–5% of intracranial aneurysms, and can occur secondary to trauma or thrombophlebitis (28,29). When a patient presents with symptoms of cavernous sinus syndrome, the diagnoses of cavernous sinus lesions or invasion by surrounding lesions should be considered first (30).

Beyond the cavernous sinus, lesions in the parasellar region include meningiomas, which are the most common primary CNS tumors; approximately 5–10% of which occur in the suprasellar and parasellar regions (31) (*Figure 6*). Additionally, craniopharyngioma is the most common suprasellar tumor in children, and the most common pediatric nonglial brain neoplasm. Other conditions, including hypothalamic hamartomas, gliomas, dermoid cysts, and epidermoid cysts, occur with lower frequency in the parasellar region.

Meckel's cave

Meckel's cave is a dural depression in the posterior fossa that protrudes into the posterior medial side of the middle cranial fossa. It is located anterior to the petrous apex of the temporal bone, and inferior to the posterior cavernous sinus that contains the CSF and the trigeminal ganglia. Meckel's cave is mainly observable by MRI, and presents a symmetrical figure-eight or an ovoid shape with CSF signals on both axial and coronal MRI images. The trigeminal ganglia are located in the lower lateral Meckel's cave but are poorly visible. The first two branches of CN V, CN V_1, and CN V_2, emerge from Meckel's cave and run along the lateral sinus wall.

The most common lesion involving Meckel's cave is trigeminal schwannoma (TS), followed by meningioma (32). Studies have demonstrated that 78–93% of TS cases involve Meckel's cave (33,34), and they often incorporate both the posterior fossa and the middle fossa, forming a dumbbell shape. In addition to the primary lesion, the specific location of Meckel's cave can induce direct infiltration and invasion of Meckel's cave by nearby sites, such as primary or metastatic lesions occurring in the cavernous sinus, dura

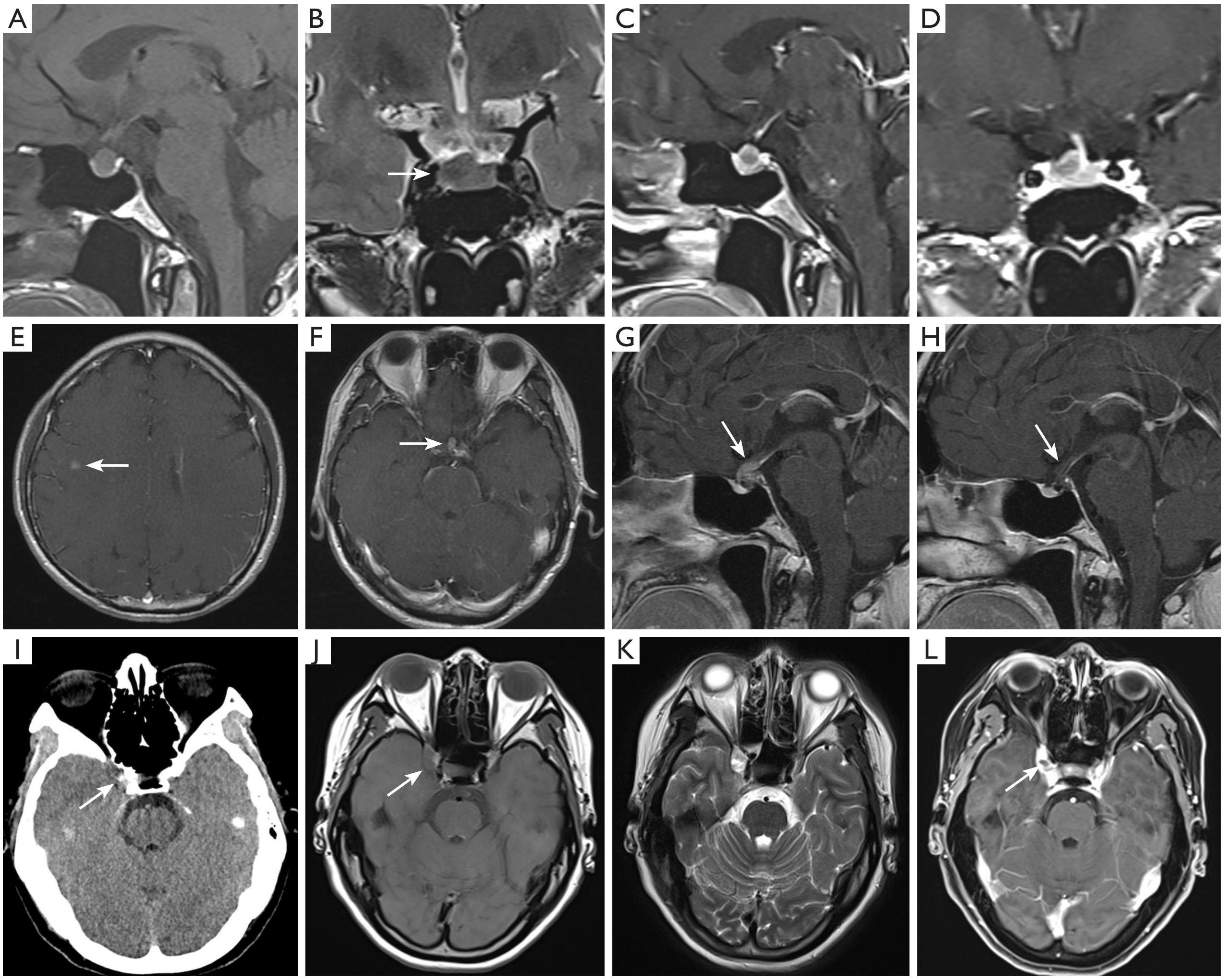

Figure 6 Blind spot in brain imaging: sella and parasellar region. (A-D) Scans of a 41-year-old female patient, who had undergone surgery for a small intestinal neuroendocrine tumor and chemotherapy for liver metastasis, and who underwent pituitary region examination to rule out multiple endocrine neoplasia. MRI revealed a nodule as slightly hypointense on T_1WI and T_2WI (arrow), while a contrast-enhanced scan showed that the nodule was less enhanced than that of the surrounding normal pituitary tissue. The pituitary stalk was shifted to the left (D), suggesting a diagnosis of a pituitary microadenoma. (E-H) Scans of a 56-year-old male patient with left upper lobe lung cancer and multiple metastases. The brain MRI revealed brain metastasis (arrow) (E); however, the thickening of the pituitary stalk in the scanned area of brain MRI was missed (arrow) (F). Due to the patient's symptoms of polydipsia and polyuria, the pituitary MRI was performed, which revealed thickening of the pituitary stalk (arrow) (G). After therapy, the lesion appeared less distinct than it had previously (arrow) (H). Follow-up confirmed the diagnosis of metastasis. (I-L) A 42-year-old female patient with a history of headache for 3 years, accompanied by right eyelid ptosis and periorbital pain. CT showed an easily missed, low-density nodule in the right parasellar region (arrow) (I). MRI revealed a scalloped nodule in the right cavernous sinus (J-L), which appeared slightly hypointense on T_1WI (arrow) (J) and mixed isointense to hyperintense on T_2WI/FS (K). Enhanced scans showed the nodule with obvious heterogeneous enhancement (arrow) (L). Postoperative pathology confirmed the diagnosis of the meningioma. MRI, magnetic resonance imaging; T_1WI, T1-weighted image; T_2WI, T2-weighted image; CT, computed tomography; FS, fat saturation.

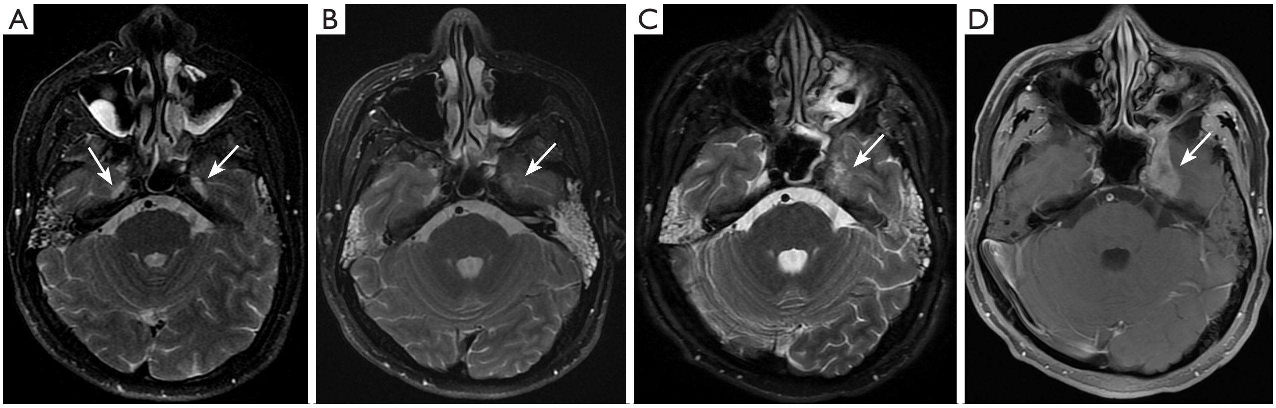

Figure 7 Blind spot in brain imaging: Meckel's cave. Scans of a 39-year-old male after radiotherapy for nasopharyngeal cancer. (A) In the initial period of follow-up, brain MRI revealed no abnormalities, and T_2WI showed symmetrical high-intensity signals resembling cerebrospinal fluid in bilateral Meckel's cave (arrows). (B) Three months later, the high-intensity signal on T_2WI in the left Meckel's cave disappeared (arrow), suggesting the possibility of recurrence. (C) In the subsequent examination, the T_2WI high-intensity signal in the left Meckel's cave was consistently not visualized, revealing the emergence of an abnormal soft tissue-like signal (arrow). (D) Enhanced scans indicated a recurrence of nasopharyngeal cancer that involved the left Meckel's cave (arrow). MRI, magnetic resonance imaging; T_2WI, T2-weighted image.

mater, pituitary gland, and skull base. More distant head and neck lesions can also infiltrate and spread through the perineural pathway to Meckel's cave. The most frequent pathway for perineural tumor progression among the divisions of CN V is V_3 (*Figure 7*). Additionally, meningeal and CSF implantation metastases are possible routes for metastatic infiltration of Meckel's cave (35).

Skull base

Basic anatomical knowledge is of vital importance for the assessment of the skull base, which is made up of five bones and apertures that transmit nerves, arteries, and veins. The five skull base bones include the occipital, temporal, pterygoid, frontal, and ethmoid bones (23). *Table 1* lists the contents and the connected anatomical sites of the skull base aperture. Clivus, a portion of the posterior cranial fossa and the posterior limit of the middle cranial fossa, is an important part that requires close attention during image interpretation. Two bones (the basisphenoid and basiocciput bones) form the clivus. The sella turcica is positioned just anterosuperior to the clivus, and the foramina lacerum is located laterally on either side. Posteriorly, the clivus slopes downward toward the foramen magnum (23).

Bone lesions of the skull base include traumatic fractures, cartilage or bone tumors, or neoplasm-like lesions (23). It has been reported that skull base fractures occur in 4–30% of head injury patients (36-38). Primary skull base tumors predominantly contain cartilage-derived tumors (chondrosarcoma and osteochondroma), chordoma, etc.; while secondary tumors include metastases, lymphomas, leukemias, and nasopharyngeal carcinoma infiltration (39); and neoplasm-like lesions include osteofibrous dysplasia and eosinophilic granulomatosis. Diagnoses of neoplastic involvement of the clivus or traumatic injury are of vital significance because they have dire consequences for patients. Assessment of the skull base through the bone window on CT is necessary, while the clivus is best assessed on MRI sagittal T_1WI (*Figure 8*), which allows for the assessment of its marrow signal intensity. In addition to the signal intensity of clival marrow, the contour and margins of the clivus can indicate tumor involvement, especially when bone erosion is present. Careful attention should also be paid to nearby structures, including the cavernous sinus and CNs, to assess for potential tumor infiltration (40). High-resolution computed tomography (HRCT) is highly recommended to clarify bone structures in skull base examinations, as HRCT clearly shows the microstructures of the skull base, especially the apertures. MRI provides a better visualization of bone marrow invasion, but sometimes the yellow bone marrow may reconvert to red bone marrow, and in such circumstances, it is difficult to differentiate this

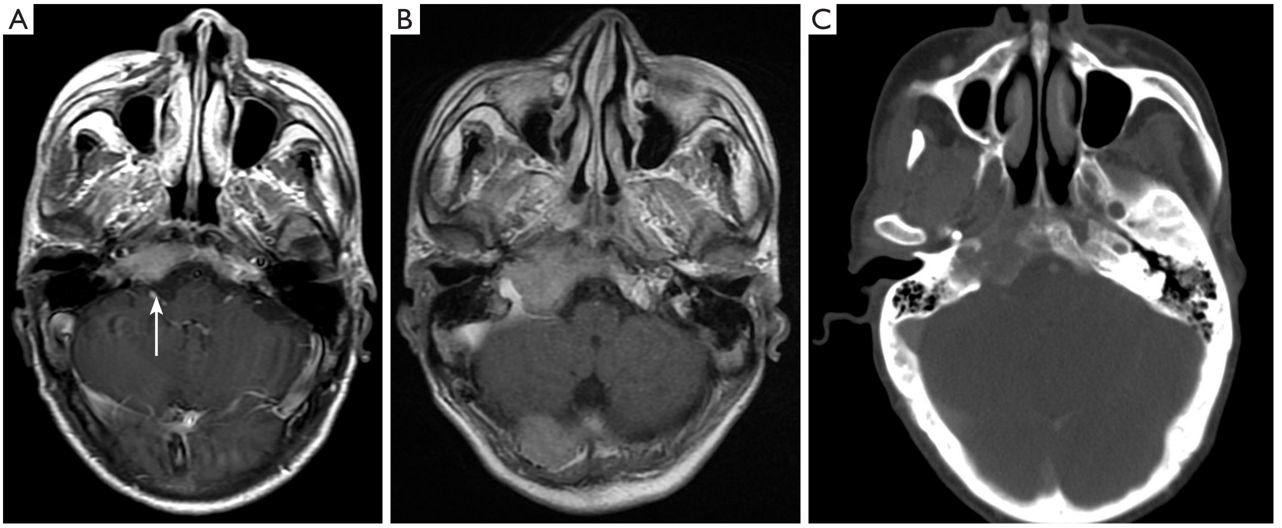

Figure 8 Blind spot in brain imaging: skull base. Scans of a 53-year-old male with hepatocellular carcinoma and orbital metastasis undergoing comprehensive treatment. To assess the efficacy of treatment for orbital metastasis, the patient underwent a brain MRI examination. (A) The MRI showed an abnormal signal lesion on the right clivus (arrow), which demonstrated a progressive enlargement during the follow-up process (B); an abnormal signal of the occipital bone was also observable in the right posterior cranial fossa (B). (C) CT bone window revealed right clivus osseous destruction. MRI, magnetic resonance imaging; CT, computed tomography.

reconversion from neoplastic involvement (40).

Scalp

The soft-tissue envelope of the skull roof is called the scalp, which extends from the protuberantia occipitalis externa and upper cervical line to the supraorbital rim, and is held in place by the ears on both sides (41). The scalp can be divided into the following five layers from superficial to deep: skin, subcutaneous tissue/superficial fascia, galea aponeurosis, sub-tendonous loose connective tissue, and cranial epithelium. On CT, the skin appears as a linear high-density area, the subcutaneous tissue appears as a fat-density area with clear margins, and the aponeurosis and muscle present as soft-tissue density areas of the same thickness. On MRI, skin and subcutaneous fat are indistinguishable, showing short T_1, long T_2 signals and uniform thickness; the aponeurosis and muscle present as isotropic T_1 and short T_2 signals, and the thickness of the different parts of the body varies but is symmetrical on both sides.

The vast majority of scalp lesions are benign. In adults, the most widely seen types are hair root sheath cysts (41%), followed by epidermal cysts, lipomas, nevi, and sebaceous cysts (41-43). In children, the most common scalp lesion is sebaceous nevus (60%), followed by infantile hemangioma, melanocytic nevus, and juvenile yellow granuloma (44,45). While the most common malignant lesions are basal cell carcinoma, squamous cell carcinoma, melanoma, Merkel cell carcinoma, and angiosarcoma (41). A direct external force can also cause scalp hematoma, which is the least severe injury in craniocerebral trauma. On CT and MRI, the scalp is usually ignored because it lies near the edge of the brain image; however, this can lead to undetected lesions (*Figure 9*). Some studies have reported that apart from the brain parenchyma, the scalp is the second most frequently overlooked region in diagnosis (46). Thus, clinical histories and physical examinations play an essential role in revealing the presence of lesions.

Orbit

The orbit, which makes up the majority of extracranial missed diagnoses (16.4% of cases), is often included in brain CT or MRI scans (46). Based on the imaging anatomy, the complicated orbital structure can be divided into the ocular region, optic nerve region, regions inside or outside the muscle cone, and subperiosteal region. Traumatic, inflammatory, and neoplastic lesions constitute the majority of ocular lesions (47). There is a close association between imaging zonation and ocular diseases, especially in neoplastic lesions (*Table 2*, *Figure 10*). Further consideration should be given to the interpretation of the orbit during

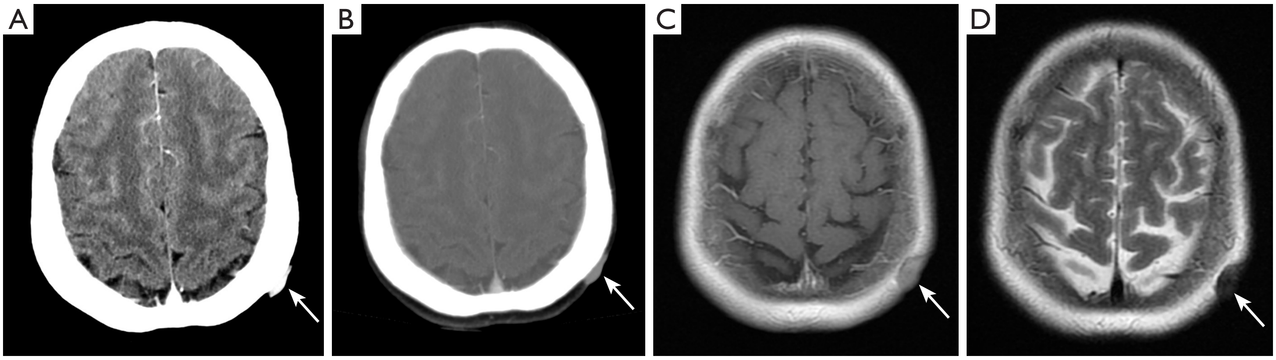

Figure 9 Blind spot in brain imaging: scalp. Scans of a 53-year-old female with multiple bone metastases, who had undergone therapy for breast cancer 5 years ago. No apparent metastases were observed in the brain parenchyma; however, radiologists missed a soft-tissue density nodule in the left scalp on CT scans (arrows) (A,B), which was more apparent on MRI images (arrows) (C,D). Subsequently, a biopsy of this nodule confirmed malignancy. Taking the patient's medical history into consideration, this nodule was highly suggestive of a metastatic lesion from breast cancer. CT, computed tomography; MRI, magnetic resonance imaging.

Table 2 Ocular imaging divisions and common lesions

Ocular imaging division	Common lesions
Eyeball region	Retinoblastoma, melanoma, metastases, etc.
Optic nerve region	Meningioma, glioma, optic neuritis, etc.
Region inside the muscle cone	Cavernous hemangioma, neurogenic tumor, etc.
Region outside the muscle cone	Lacrimal gland tumor, inflammatory pseudotumor, lymphoma, neurogenic tumor, etc.
Subperiosteal region	Hematoma, dermoid/epidermoid cyst, flat hypertrophic meningioma, metastases, etc.

brain imaging examinations, as ocular lesions can be easily missed and misdiagnosed due to a lack of pertinent information, or clinicians focusing primarily on intracranial lesions.

PPF

Brain CT or MRI include some of the cervicofacial structures, as well as abnormalities in adjacent areas such as the sinuses and nasopharynx, and atypical places such as the PPF. The PPF is a pair of narrow bony spaces located at the base of the anterior fossa on both sides, inside the infratemporal fossa, behind the infraorbital apex, and surrounded by the maxillary body, pterygoid process of the sphenoid bone, and palatine bone (48). It contains the pterygopalatine ganglion, the maxillary nerve, the pterygopalatine nerve, and the maxillary artery (49). The PPF communicates directly with seven intracranial and extracranial sites via eight channels: forward to the orbit via the inferior orbital fissure; posteriorly upward to the middle fossa via the foramen roundum; posteriorly downward to the pharynx via the palatine sheath canal; posteriorly inward to the foramen lacerum via the pterygopalatine ducts; inward to the nasal cavity via the foramen of the pterygopalatine; outward via pterygomaxillary fissure to the infratemporal fossa; and downward to the oral cavity via the pterygopalatine canal, foramina palatine majora, and foramina palatine minora. The preferred method for assessing the various bone anatomical features of the PPF is HRCT (48,50), but MRI is superior at detecting pathological changes in the PPF, especially PNS (49).

The PPF is a critical route of disease transmission, and PPF lesions are usually caused by malignancies or the inflammatory invasion of neighboring structures, and are rare as primary lesions. The primary lesions penetrating the PPF include sellar region lesions, while orbital, nasal, and sinus lesions are the most frequently encountered extracranial lesions (*Figure 11*) (51,52). Further, fibrous hemangiomas and schwannomas are the most typical varieties of primary tumors (53).

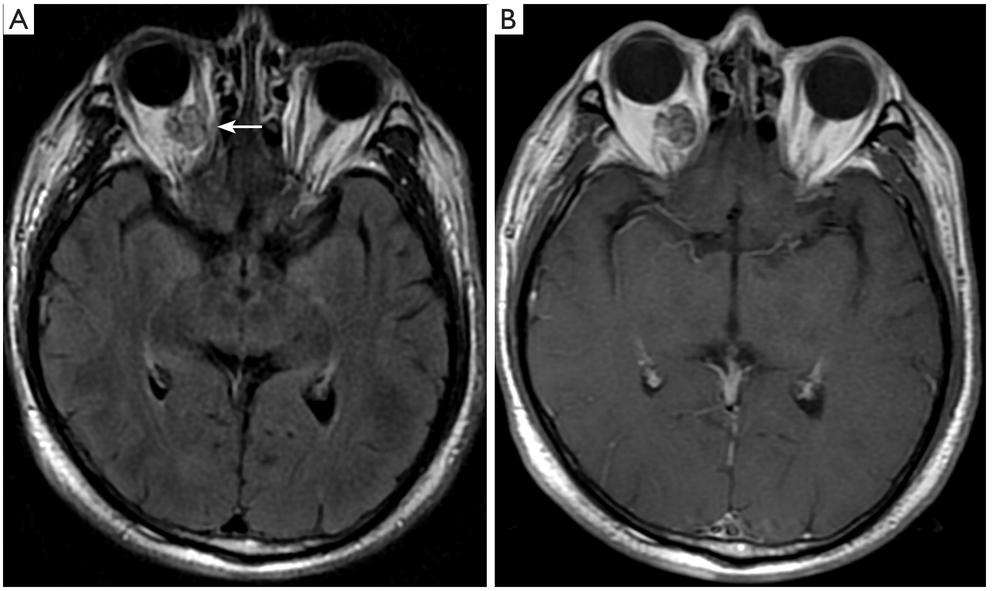

Figure 10 Blind spot in brain imaging: orbit. Scans of a 58-year-old male after surgery for adenocarcinoma of the left upper lung lobe. (A) MRI revealed the presence of an abnormal signal nodule in the right orbit (arrow), exhibiting mild and uneven enhancement on contrast-enhanced scans with clear boundaries. (B) Throughout the follow-up process, no distinct changes were observed, leading to the consideration of a benign condition, possibly a cavernous sinus hemangioma. MRI, magnetic resonance imaging.

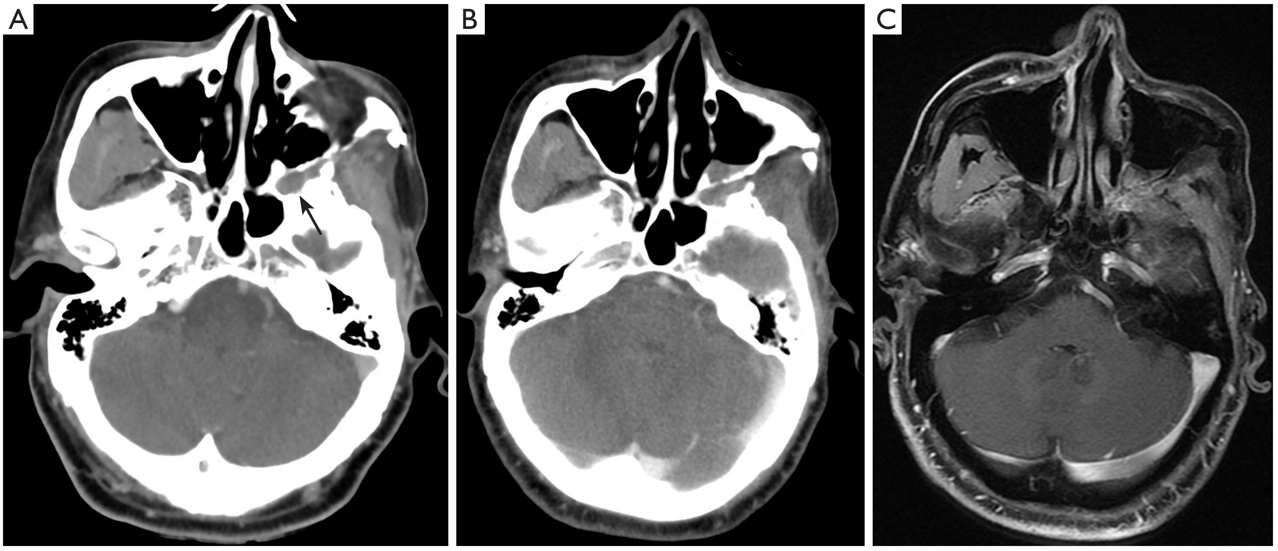

Figure 11 Blind spot in brain imaging: pterygopalatine fossa. Scans of a 54-year-old male after adenoid cystic carcinoma in the left orbital apex. (A) During early follow-up, mild enlargement of the pterygopalatine fossa (arrow) suggested a potential lesion. (B,C) During the follow-up process, there was a gradual enlargement of the pterygopalatine fossa. Simultaneously, soft-tissue shadows were detected in the left orbital apex and pterygopalatine fossa, exhibiting uneven enhancement on contrast-enhanced scans. Ultimately, a diagnosis of tumor recurrence was made.

Systematic strategies for missed diagnostic errors in radiology

In this article, we summarized and discussed common diagnostic blind spots in cranial radiology, providing key considerations for each area, as well as common diagnoses and differential diagnoses. For instance, when evaluating the skull base, we emphasized the importance of closely examining the clivus for neoplastic or traumatic involvement, as such conditions can have severe consequences for patients. We then pointed out that sagittal T_1WI MRI is the most effective tool for assessing the clivus.

However, in clinical practice, the time radiologists have to read massive images is always limited, thus perceptual errors are inevitable despite the extensive training of radiologists. To mitigate these errors, alternative strategies can also be employed, such as improving imaging protocol selection, using a multiple reviewer report system, using structured reporting templates, and using error measurement or detection strategies such as electronic trigger tools and checklists to detect "wrong-side" misidentification errors (54,55).

In recent years, significant advances in the use of artificial intelligence (AI) have transformed many radiology applications in clinical work, from medical image interpretation to clinical and operational decision making. AI software has been widely used for lung and breast nodule detection. Additionally, brain imaging studies have shown that AI has the potential to detect brain abnormalities. Swinburne *et al.* developed a brain MRI tumor detection model that uses mined annotations, significantly enhancing tumor detection capabilities. Similarly, Gauriau *et al.* introduced a deep learning-based model to detect abnormalities in brain MRI scans, showcasing its potential as a triage tool to improve the efficiency of the radiology department (56,57). However, AI detection in brain diseases is still in the experimental stage, and has not yet been extensively integrated into routine clinical practice. Consequently, to implement continuous learning AI, radiology departments will need to co-develop and test AI algorithms, provide continuous data feeds, and integrate more diverse data sources (58).

Conclusions

This review summarized the blind spots that are easily missed when reading brain imaging scans, including scans of the posterior fossa, cerebral sulci and pia mater, CNs, intracranial arteries, dural sinuses, sella and parasellar region, Meckel's cave, skull base, scalp, orbit, and PPF. This review also provided solutions to help radiologists reduce missed diagnoses in daily work. This article also has continuing education implications for junior doctors.

Acknowledgments

Funding: This study was supported by CAMS Innovation Fund for Medical Science (No. 2011-1-12M-012).

Footnote

Conflicts of Interest: All authors have completed the ICMJE uniform disclosure form (available at https://qims.amegroups.com/article/view/10.21037/qims-24-1270/coif). The authors have no conflicts of interest to declare.

Ethical Statement: The authors are accountable for all aspects of the work in ensuring that questions related to the accuracy or integrity of any part of the work are appropriately investigated and resolved.

References

1. Bruno MA, Walker EA, Abujudeh HH. Understanding and Confronting Our Mistakes: The Epidemiology of Error in Radiology and Strategies for Error Reduction. Radiographics 2015;35:1668-76.
2. Kim YW, Mansfield LT. Fool me twice: delayed diagnoses in radiology with emphasis on perpetuated errors. AJR Am J Roentgenol 2014;202:465-70.
3. Berlin L. Malpractice issues in radiology. Perceptual errors. AJR Am J Roentgenol 1996;167:587-90.
4. Bonneville F, Savatovsky J, Chiras J. Imaging of cerebellopontine angle lesions: an update. Part 1: enhancing extra-axial lesions. Eur Radiol 2007;17:2472-82.
5. Bonneville F, Savatovsky J, Chiras J. Imaging of

cerebellopontine angle lesions: an update. Part 2: intra-axial lesions, skull base lesions that may invade the CPA region, and non-enhancing extra-axial lesions. Eur Radiol 2007;17:2908-20.
6. Chandrasoma P, Taylor CR. Concise pathology. 3rd edition. Stamford, CT, USA: Appleton & Lange; 1998.
7. Pereira FV, Jarry VM, Castro JTS, Appenzeller S, Reis F. Pediatric inflammatory demyelinating disorders and mimickers: How to differentiate with MRI? Autoimmun Rev 2021;20:102801.
8. Hesselink JR, Healy ME, Press GA, Brahme FJ. Benefits of Gd-DTPA for MR imaging of intracranial abnormalities. J Comput Assist Tomogr 1988;12:266-74.
9. Adeeb N, Mortazavi MM, Deep A, Griessenauer CJ, Watanabe K, Shoja MM, Loukas M, Tubbs RS. The pia mater: a comprehensive review of literature. Childs Nerv Syst 2013;29:1803-10.
10. Kamran S, Bener AB, Alper D, Bakshi R. Role of fluid-attenuated inversion recovery in the diagnosis of meningitis: comparison with contrast-enhanced magnetic resonance imaging. J Comput Assist Tomogr 2004;28:68-72.
11. Gaeta M, Galletta K, Cavallaro M, Mormina E, Cannizzaro MT, Lanzafame LRM, D'Angelo T, Blandino A, Vinci SL, Granata F. T1 relaxation: Chemo-physical fundamentals of magnetic resonance imaging and clinical applications. Insights Imaging 2024;15:200.
12. Montejo C, Laredo C, Llull L, Martínez-Heras E, López-Rueda A, Torné R, Garrido C, Bargallo N, Llufriu S, Amaro S. Synthetic MRI in subarachnoid haemorrhage. Clin Radiol 2021;76:785.e17-23.
13. Mahendru G, Chong V. Meninges in cancer imaging. Cancer Imaging 2009;9 Spec No A:S14-21.
14. Traylor KS, Branstetter BF 4th. Cranial Nerve Anatomy. Neuroimaging Clin N Am 2022;32:565-76.
15. Romano N, Federici M, Castaldi A. Imaging of cranial nerves: a pictorial overview. Insights Imaging 2019;10:33.
16. Hwang JY, Yoon HK, Lee JH, Yoon HM, Jung AY, Cho YA, Lee JS, Yoon CH. Cranial Nerve Disorders in Children: MR Imaging Findings. Radiographics 2016;36:1178-94.
17. Modi T, Verma M, Patkar D. Multiple Cranial Nerve Involvement as a Presentation of Primary Central Nervous System Lymphoma: A Case-Based Review. Asian J Neurosurg 2021;16:835-40.
18. Klimaj Z, Klein JP, Szatmary G. Cranial Nerve Imaging and Pathology. Neurol Clin 2020;38:115-47.
19. Sheth S, Branstetter BF 4th, Escott EJ. Appearance of normal cranial nerves on steady-state free precession MR images. Radiographics 2009;29:1045-55.
20. Qureshi AI, Caplan LR. Intracranial atherosclerosis. Lancet 2014;383:984-98.
21. Jakanani GC, Aslam M, Rao B. Basilar artery: another anatomic blind spot at brain imaging. Radiographics 2010;30:1431-2.
22. Gounis MJ, van der Marel K, Marosfoi M, Mazzanti ML, Clarençon F, Chueh JY, Puri AS, Bogdanov AA Jr. Imaging Inflammation in Cerebrovascular Disease. Stroke 2015;46:2991-7.
23. Bahrami S, Yim CM. Quality initiatives: blind spots at brain imaging. Radiographics 2009;29:1877-96.
24. Oliveira IM, Duarte JÁ, Dalaqua M, Jarry VM, Pereira FV, Reis F. Cerebral venous thrombosis: imaging patterns. Radiol Bras 2022;55:54-61.
25. Buyck PJ, Zuurbier SM, Garcia-Esperon C, Barboza MA, Costa P, Escudero I, et al. Diagnostic accuracy of noncontrast CT imaging markers in cerebral venous thrombosis. Neurology 2019;92:e841-51.
26. Jipa A, Jain V. Imaging of the sellar and parasellar regions. Clin Imaging 2021;77:254-75.
27. Kameda-Smith MM, Zhang E, Lannon M, Algird A, Reddy K, Lu JQ. Pituitary metastasis: From pathology to clinical and radiological considerations. J Clin Neurosci 2021;93:231-40.
28. Tang Y, Booth T, Steward M, Solbach T, Wilhelm T. The imaging of conditions affecting the cavernous sinus. Clin Radiol 2010;65:937-45.
29. Razek AA, Castillo M. Imaging lesions of the cavernous sinus. AJNR Am J Neuroradiol 2009;30:444-52.
30. Housley SB, McPheeters MJ, Raygor KP, Bouslama M, Scullen T, Davies JM. Cavernous Sinus Thrombosis. Neurosurg Clin N Am 2024;35:305-10.
31. Kirsch CFE. Imaging of Sella and Parasellar Region. Neuroimaging Clin N Am 2021;31:541-52.
32. Beck DW, Menezes AH. Lesions in Meckel's cave: variable presentation and pathology. J Neurosurg 1987;67:684-9.
33. Youssef S, Kim EY, Aziz KM, Hemida S, Keller JT, van Loveren HR. The subtemporal interdural approach to dumbbell-shaped trigeminal schwannomas: cadaveric prosection. Neurosurgery 2006;59:ONS270-7; discussion ONS277-8.
34. Yoshida K, Kawase T. Trigeminal neurinomas extending into multiple fossae: surgical methods and review of the literature. J Neurosurg 1999;91:202-11.
35. Kamel HA, Toland J. Trigeminal nerve anatomy: illustrated using examples of abnormalities. AJR Am J Roentgenol 2001;176:247-51.

36. Dreizin D, Sakai O, Champ K, Gandhi D, Aarabi B, Nam AJ, Morales RE, Eisenman DJ. CT of Skull Base Fractures: Classification Systems, Complications, and Management. Radiographics 2021;41:762-82.
37. Bell RB, Chen J. Frontobasilar fractures: contemporary management. Atlas Oral Maxillofac Surg Clin North Am 2010;18:181-96.
38. Stone JA, Castillo M, Neelon B, Mukherji SK. Evaluation of CSF leaks: high-resolution CT compared with contrast-enhanced CT and radionuclide cisternography. AJNR Am J Neuroradiol 1999;20:706-12.
39. Hsiung CY, Wu JM, Wang CJ, Kuo SC, Yeh SA, Hsu HC, Huang EY. Attenuation of radiation dose by the skull base bone in patients with nasopharyngeal carcinoma: clinical importance. Radiology 2001;218:457-63.
40. Kimura F, Kim KS, Friedman H, Russell EJ, Breit R. MR imaging of the normal and abnormal clivus. AJR Am J Roentgenol 1990;155:1285-91.
41. Kawaguchi M, Kato H, Matsuo M. CT and MRI features of scalp lesions. Radiol Med 2019;124:1049-61.
42. Prodinger CM, Koller J, Laimer M. Scalp tumors. J Dtsch Dermatol Ges 2018;16:730-53.
43. Türk CÇ, Bacanlı A, Kara NN. Incidence and clinical significance of lesions presenting as a scalp mass in adult patients. Acta Neurochir (Wien) 2015;157:217-23.
44. Yang CC, Chen YA, Tsai YL, Shih IH, Chen W. Neoplastic skin lesions of the scalp in children: a retrospective study of 265 cases in Taiwan. Eur J Dermatol 2014;24:70-5.
45. Yoon SH, Park SH. A study of 77 cases of surgically excised scalp and skull masses in pediatric patients. Childs Nerv Syst 2008;24:459-65.
46. Tu LH, Bokhari SAJ. Blind spots on CT imaging of the head: Insights from 5 years of report addenda at a single institution. Clin Imaging 2021;76:189-94.
47. Tailor TD, Gupta D, Dalley RW, Keene CD, Anzai Y. Orbital neoplasms in adults: clinical, radiologic, and pathologic review. Radiographics 2013;33:1739-58.
48. Erdogan N, Unur E, Baykara M. CT anatomy of pterygopalatine fossa and its communications: a pictorial review. Comput Med Imaging Graph 2003;27:481-7.
49. Tashi S, Purohit BS, Becker M, Mundada P. The pterygopalatine fossa: imaging anatomy, communications, and pathology revisited. Insights Imaging 2016;7:589-99.
50. Daniels DL, Rauschning W, Lovas J, Williams AL, Haughton VM. Pterygopalatine fossa: computed tomographic studies. Radiology 1983;149:511-6.
51. Kuo YH, Lin CS. Regression of advanced maxillary sinus cancer with orbital invasion by combined chemotherapy and immunotherapy: A one-year follow-up case report. Mol Clin Oncol 2022;16:94.
52. Zhou B, Tang Z, Lv L, Yu J, Li X, Yang C, Xiang S, Song Z, Zhang D. The application of 3-dimensional magnetic resonance imaging in nasopharyngeal carcinoma with pterygopalatine fossa invasion. Magn Reson Imaging 2023;96:38-43.
53. Zalzal HG, Turner MT. Robotic-assisted transmaxillary approach for removal of juvenile nasopharyngeal angiofibroma of the pterygopalatine and infratemporal fossa. Head Neck 2020;42:2745-9.
54. Zhang L, Wen X, Li JW, Jiang X, Yang XF, Li M. Diagnostic error and bias in the department of radiology: a pictorial essay. Insights Imaging 2023;14:163.
55. Sheehan SE, Safdar N, Singh H, Sittig DF, Bruno MA, Keller K, Kinnard S, Brunner MC. Detection and Remediation of Misidentification Errors in Radiology Examination Ordering. Appl Clin Inform 2020;11:79-87.
56. Swinburne NC, Yadav V, Kim J, Choi YR, Gutman DC, Yang JT, Moss N, Stone J, Tisnado J, Hatzoglou V, Haque SS, Karimi S, Lyo J, Juluru K, Pichotta K, Gao J, Shah SP, Holodny AI, Young RJ; MSK MIND Consortium. Semisupervised Training of a Brain MRI Tumor Detection Model Using Mined Annotations. Radiology 2022;303:80-9.
57. Gauriau R, Bizzo BC, Kitamura FC, Landi Junior O, Ferraciolli SF, Macruz FBC, Sanchez TA, Garcia MRT, Vedolin LM, Domingues RC, Gasparetto EL, Andriole KP. A Deep Learning-based Model for Detecting Abnormalities on Brain MR Images for Triaging: Preliminary Results from a Multisite Experience. Radiol Artif Intell 2021;3:e200184.
58. Pianykh OS, Langs G, Dewey M, Enzmann DR, Herold CJ, Schoenberg SO, Brink JA. Continuous Learning AI in Radiology: Implementation Principles and Early Applications. Radiology 2020;297:6-14.

Cite this article as: Liu M, Wen X, Li M, Huang Q, Jiang C, Jiang J, Zhang L, Zhang H. Blind spots in brain imaging: a pictorial essay. Quant Imaging Med Surg 2025;15(1):1023-1039. doi: 10.21037/qims-24-1270

